



Cite as  
Nano-Micro Lett.  
(2023) 15:166

Received: 15 March 2023  
Accepted: 19 May 2023  
Published online: 3 July 2023  
© The Author(s) 2023

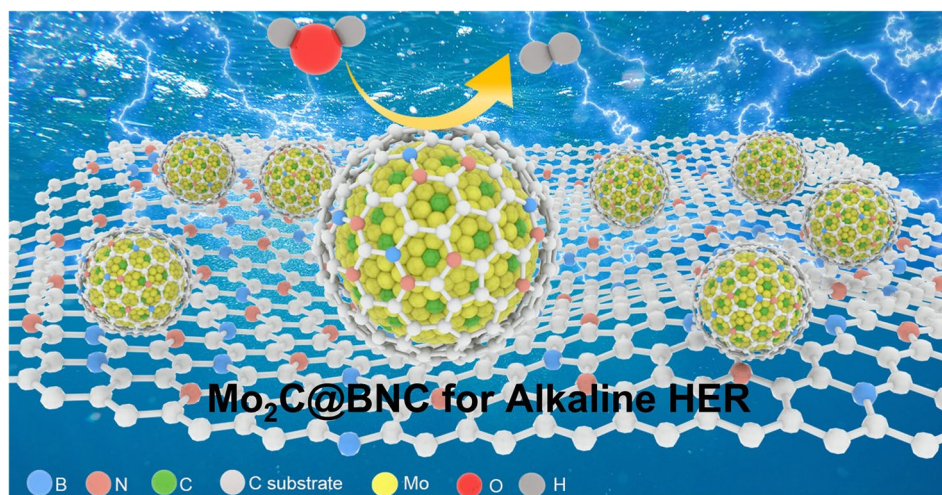
## Synergistic Effect of Dual-Doped Carbon on Mo<sub>2</sub>C Nanocrystals Facilitates Alkaline Hydrogen Evolution

Min Zhou<sup>1,3</sup> ✉, Xiaoli Jiang<sup>1,2</sup>, Weijie Kong<sup>3</sup>, Hangfei Li<sup>3</sup>, Fei Lu<sup>3</sup>, Xin Zhou<sup>4</sup>,  
Yagang Zhang<sup>1,2</sup> ✉

### HIGHLIGHTS

- The B and N dual-doped carbon layer that encapsulated on Mo<sub>2</sub>C nanocrystals (Mo<sub>2</sub>C@BNC) were fabricated for accelerating HER under alkaline condition.
- Theoretical calculations reveal that the H<sub>2</sub>O could be decomposed spontaneously over the introduced B sites, and the defective C atoms in the dual-doped carbon layer provide the best H binding sites.
- The optimized dual doped Mo<sub>2</sub>C catalyst with synergistic effect of non-metal sites delivers superior HER performances.

**ABSTRACT** Molybdenum carbide (Mo<sub>2</sub>C) materials are promising electrocatalysts with potential applications in hydrogen evolution reaction (HER) due to low cost and Pt-like electronic structures. Nevertheless, their HER activity is usually hindered by the strong hydrogen binding energy. Moreover, the lack of water-cleaving sites makes it difficult for the catalysts to work in alkaline solutions. Here, we designed and synthesized a B and



N dual-doped carbon layer that encapsulated on Mo<sub>2</sub>C nanocrystals (Mo<sub>2</sub>C@BNC) for accelerating HER under alkaline condition. The electronic interactions between the Mo<sub>2</sub>C nanocrystals and the multiple-doped carbon layer endow a near-zero H adsorption Gibbs free energy on the defective C atoms over the carbon shell. Meanwhile, the introduced B atoms afford optimal H<sub>2</sub>O adsorption sites for the water-cleaving step. Accordingly, the dual-doped Mo<sub>2</sub>C catalyst with synergistic effect of non-metal sites delivers superior HER performances of a low overpotential (99 mV@10 mA cm<sup>-2</sup>) and a small Tafel slope (58.1 mV dec<sup>-1</sup>) in 1 M KOH solution. Furthermore, it

✉ Min Zhou, minzhou@yzu.edu.cn; Yagang Zhang, ygzhang@uestc.edu.cn

<sup>1</sup> School of Materials and Energy, University of Electronic Science and Technology of China, Chengdu 611731, People's Republic of China

<sup>2</sup> State Key Laboratory of Electronic Thin Films and Integrated Devices, University of Electronic Science and Technology of China, Chengdu 610054, People's Republic of China

<sup>3</sup> College of Physical Science and Technology, Yangzhou University, Yangzhou 225002, People's Republic of China

<sup>4</sup> Department of Chemical Engineering, Polytechnique Montréal, Montréal, QC H3C 3A7, Canada



presents a remarkable activity that outperforming the commercial 10% Pt/C catalyst at large current density, demonstrating its applicability in industrial water splitting. This study provides a reasonable design strategy towards noble-metal-free HER catalysts with high activity.

**KEYWORDS** Molybdenum carbide; Hydrogen evolution reaction; Dual-doped; Synergistic effect; Superior performances

## 1 Introduction

To address the threats of the energy crisis and environmental pollution from the increasing utilization of fossil fuels, great efforts have been devoted to exploring clean and renewable energy sources [1, 2]. Hydrogen, due to its high energy density, non-polluting and renewable features, has long been advocated as an excellent alternative to fossil fuels [3–5]. Electrocatalytic water splitting is considered as the most promising and desirable technology by researchers and entrepreneurs for hydrogen production [6–8]. So far, noble-metal-based materials (such as Pt, Ir and Ru-based catalysts) have been extensively investigated for hydrogen production. Unfortunately, the scarcity and high price limit their broad applications [9–14]. Therefore, one of the crucial tasks is the development of low-cost and high-performance noble-metal-free catalysts.

Molybdenum carbide ( $\text{Mo}_2\text{C}$ ) is emerging as an excellent replacement for the noble-metal-based catalysts by the virtue of low-cost and platinum-like electronic structure [15–18]. Recently, Yang et al. [19] proposed a novel coral-like porous nitrogen-doped  $\text{Mo}_2\text{C}$  electrocatalyst (3D  $\text{Mo}_2\text{C}$ ) as HER electrocatalyst, which displayed an overpotential of 110 mV and a small Tafel slope of  $73.9 \text{ mV dec}^{-1}$  in 1 M KOH. Nevertheless, the strong hydrogen binding energy (HBE) of  $\text{Mo}_2\text{C}$  hinders the further improvement of the HER activity, as the density of the *d*-orbital vacancies of Mo is relatively high [20, 21]. This favors the hydrogen adsorption process (Volmer step), but severely hampers the hydrogen desorption process (Heyrovsky or Tafel step) in HER processes.

Previous literatures have shown that coupling  $\text{Mo}_2\text{C}$  with other transition metals (such as Co and Ni) is conducive to significantly enhance the HER performance via tuning the adsorption strength of the Mo–H bond [22, 23]. However, the metal dopants may suffer from dissolution issues in the electrolytes, causing ungratified stability. In this regard, carbon encapsulation onto the  $\text{Mo}_2\text{C}$  can significantly improve the stability of the catalyst [24–26]. Meanwhile, a few studies shown that the exterior carbon can be activated by the interactions between  $\text{Mo}_2\text{C}$  and the carbon encapsulated [27, 28]. More

importantly, the alkaline HER kinetics is usually restricted by the water dissociation step, which may affect the whole reaction rate [29]. Therefore, the absence of water dissociation sites in  $\text{Mo}_2\text{C}$  catalysts limited the further enhancement of the HER performance in alkaline medias. B-doping is previously proposed to benefit the water dissociation process. The electron-deficient B adsorbs water by coordinating with lone pair electrons, which weakens the O–H bond and thus accelerate the water dissociation step. For instance, Liu and Sun's group demonstrated that B dopants in Ru NCs/BNG effectively boost the dissociation of water and facilitate the HER reaction rate [30].

Inspired by the previous results, this work reports the synthesis of B, N dual-doped carbon layer encapsulated on  $\text{Mo}_2\text{C}$  nanocrystals ( $\text{Mo}_2\text{C}@BNC$ ) via a facile one-pot pyrolysis method for alkaline HER. The introduced B atom in the carbon layer is aimed to optimize the carbon shell electronic structures for  $\text{H}_2\text{O}$  adsorption. As expected, the prepared  $\text{Mo}_2\text{C}@BNC$  catalyst displays remarkable electrocatalytic activity towards HER under alkaline conditions. More importantly, the catalytic activity is even higher than that of the commercial 10% Pt/C catalyst at large current density. Theoretical calculations reveal that the  $\text{H}_2\text{O}$  could be decomposed spontaneously over the introduced B sites, and the defective C atoms in the dual-doped carbon layer provide the best H binding sites. The synergistic effect between the non-metal sites (B and C) on the carbon shell optimize the rates of Volmer and Heyrovsky reaction, simultaneously, leading to the superb performance of the catalyst.

## 2 Experimental Methods

### 2.1 Experimental Reagents

Ammonium molybdate tetrahydrate ( $(\text{NH}_4)_6\text{Mo}_7\text{O}_{24}\cdot 4\text{H}_2\text{O}$ ), dicyandiamide ( $\text{C}_2\text{H}_4\text{N}_4$ ), boric acid ( $\text{H}_3\text{BO}_3$ ), KOH are analytical grade and without further purification. Millipore water (resistivity:  $\sim 18 \text{ M}\Omega \text{ cm}$ ) was used in all experiments.

## 2.2 Synthesis of Mo<sub>2</sub>C@BNC

Mo<sub>2</sub>C@BNC was synthesized via two steps. First, 1 g of C<sub>2</sub>H<sub>4</sub>N<sub>4</sub> was dissolved in 10 mL of deionized water, stirred for 15 min, then added 50 mg of (NH<sub>4</sub>)<sub>6</sub>Mo<sub>7</sub>O<sub>24</sub>·4H<sub>2</sub>O with 5 mg of H<sub>3</sub>BO<sub>3</sub>, heated and stirred until a white crystalline powder was formed. The white crystalline powder was collected and ground in an agate mortar for 15 min. In the second step, the powder was heated under an H<sub>2</sub>/Ar (5:95) atmosphere at 500 °C for 30 min with a heating rate of 5 °C min<sup>-1</sup>, then heated at 800 °C for another 6 h with a heating rate of 10 °C min<sup>-1</sup>.

## 2.3 Synthesis of Mo<sub>2</sub>C@NC

The Mo<sub>2</sub>C@NC was prepared using the same method as the Mo<sub>2</sub>C@BNC except that the H<sub>3</sub>BO<sub>3</sub> was not added.

## 2.4 Synthesis of Mo<sub>2</sub>C@C

50 mg of (NH<sub>4</sub>)<sub>6</sub>Mo<sub>7</sub>O<sub>24</sub>·4H<sub>2</sub>O was mixed with 1 g of glucose and ground in an agate mortar for 15 min, then the homogeneous mixture was placed in a quartz tube and heated under an Ar atmosphere at 800 °C for 6 h with a heating rate of 5 °C min<sup>-1</sup>.

## 2.5 Materials Characterizations

The phase structures of all samples were identified by Shimadzu X-ray diffraction (XRD)-7000 powder X-ray diffractometer (Cu Ka). The morphologies and structures of the products were characterized by Tecnai G2 F30 S-TWIN transmission electron microscopy (TEM). X-ray photoelectron spectroscopy (XPS) measurements were performed on a Thermo ESCALAB250Xi spectrometer with a resolution of 0.43 eV. Raman measurements were executed on a Renishaw inVia Raman spectrometer with a spectral range of 10~4000 cm<sup>-1</sup>. Fourier transform infrared spectroscopy (FT-IR) measurements were carried out on a Varian infrared spectrometer model Cary 670-IR with a wave number ranging from 4000 to 400 cm<sup>-1</sup>. The contact angle (CA) of the electrocatalysts on the electrode surface were measured using a contact angle meter (JY-82C).

## 2.6 Electrochemical Measurements

The electrocatalytic activity was evaluated in a three-electrode system with 1 M KOH as electrolyte using a CHI 760E electrochemistry workstation (Chenhua, Shanghai). To obtain homogeneous ink, 1.2 mg acetylene black and 4.8 mg of sample were dispersed in 300 μL of ethanol and 30 μL of Nafion. The mixture was ultrasonicated for about 20 min, then added 300 μL of deionized water and sonicated for another 20 min. Next, 9 μL of the catalyst dispersion (8 mg mL<sup>-1</sup>) was loaded onto a glassy carbon electrode (0.1256 cm<sup>2</sup> of area) and then dried at 60 °C for 10 min serving as the working electrode. In this case, the above prepared Mo<sub>2</sub>C@BNC was formulated as an ink drop on a L-shaped glassy carbon electrode (4 mm diameter) as the working electrode (the loading mass of Mo<sub>2</sub>C@BNC is 0.54 mg cm<sup>-2</sup>). Linear sweep voltammetry (LSV) was performed at a scan rate of 5 mV s<sup>-1</sup>. Electrochemical impedance spectroscopy (EIS) was performed at a cathode bias of -0.2 V versus RHE, using a sinusoidal voltage of 5 mV in the range of 100 kHz-0.1 Hz. At 0.1-0.2 V versus RHE region, a series of CV measurements were performed at different sweep rates (10, 20, 40, 60, 80, 100 mV s<sup>-1</sup>). Stability was tested at 10 mA cm<sup>-2</sup> for constant current V-t curves. The polarization curves normalized by ECSA was calculated on the basis of previous report with some modifications [31]. Firstly, C<sub>dl</sub> determined from the slope of the plot between the charging current *i* and scan rate *v* (C<sub>dl</sub> = *i/v*). Then, the ECSA calculated by dividing C<sub>dl</sub> by specific capacitance (ECSA = C<sub>dl</sub>/C<sub>s</sub>). Here, the specific capacitances (C<sub>s</sub>) were chosen as C<sub>s</sub> = 0.04 mF cm<sup>-2</sup> based on typical reported values. Finally, the LSV curve was normalized by using the ECSA data obtained above.

## 2.7 Density Functional Theory (DFT) Calculations

All DFT calculations were performed in the Vienna ab initio simulation package (VASP) using projector-augmented wave (PAW) potentials. The exchange-correlation energy is described by the generalized gradient approximation (GGA) with *Perdew-Burke-Ernzerhof* (PBE) functional. The cut-off value of the plane wave basis set is set to 400 eV. We employed a slab model where the vacuum spacing perpendicular to the surface layer is larger than 15 Å to eliminate physical interactions due to periodic boundary conditions

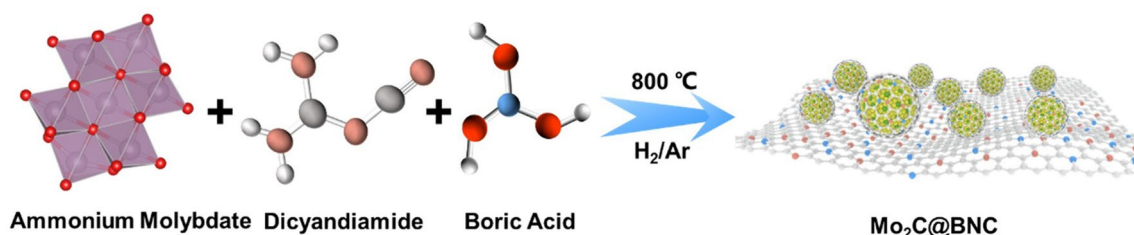


**Fig. 1** Schematic of synthesis N, B dual-doped Mo<sub>2</sub>C nanocrystals (Mo<sub>2</sub>C@BNC)

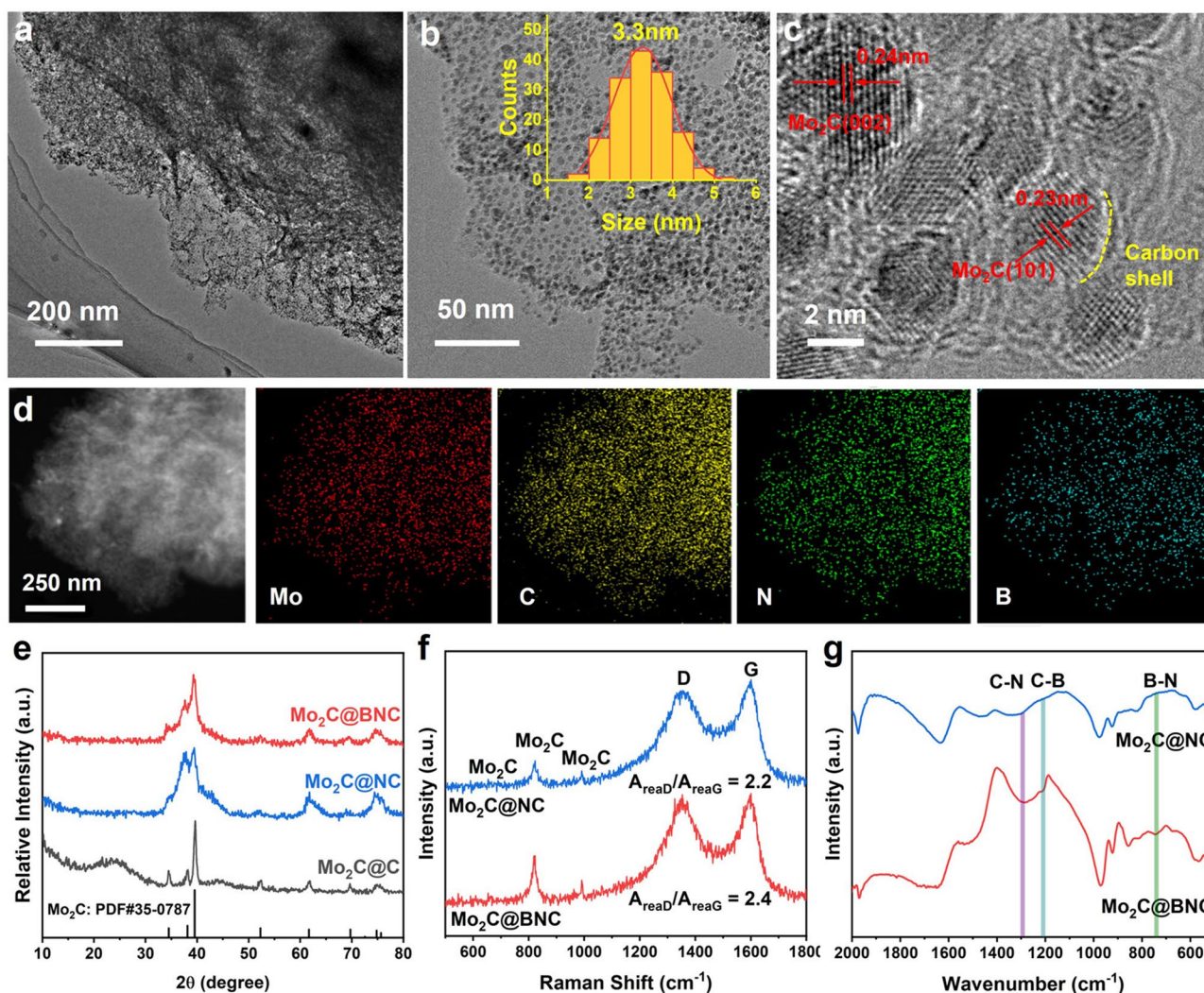


**Fig. 2** Structural characterization of the materials. **a**, **b** TEM images of the Mo<sub>2</sub>C@BNC, inset of **b**: the particle size distribution of the Mo<sub>2</sub>C nanocrystals. **c** HRTEM images of the Mo<sub>2</sub>C@BNC. **d** Elemental mapping of the Mo<sub>2</sub>C@BNC. **e** XRD pattern of the Mo<sub>2</sub>C@C, Mo<sub>2</sub>C@NC, and Mo<sub>2</sub>C@BNC. **f** Raman spectra of the Mo<sub>2</sub>C@NC and Mo<sub>2</sub>C@BNC. **g** FT-IR spectra of the Mo<sub>2</sub>C@NC and Mo<sub>2</sub>C@BNC

along this direction. The convergence threshold of the force is reached when the Hellmann–Feynman force on each atom is less than  $0.01 \text{ eV } \text{Å}^{-1}$ .  $2 \times 2 \times 1$  and  $5 \times 5 \times 1$   $\Gamma$ -centered

$k$ -grids are used for geometric optimization and electronic structure calculations.

### 3 Results and Discussion

#### 3.1 Catalyst Design and Structural Characterization

Mo<sub>2</sub>C@BNC was synthesized by a convenient one-pot pyrolysis method, in which ammonium molybdate tetrahydrate, dicyandiamide and boric acid were utilized as the raw materials (Fig. 1). The morphology of the sample was characterized by TEM and High-resolution TEM (HR-TEM). Figure 2a–b shows a foam-like structure of the Mo<sub>2</sub>C@BNC, in which Mo<sub>2</sub>C nanocrystals are uniformly distributed on the BNC substrate [32]. The inset of Fig. 2b displays the average particle size of ~3.3 nm for the Mo<sub>2</sub>C nanocrystals. The lattice spacing of 0.23 and 0.24 nm correspond to the (101) and (002) crystal planes of the Mo<sub>2</sub>C, respectively (Fig. 2c). Moreover, the Mo<sub>2</sub>C nanocrystals are found to be encapsulated by an ultrathin carbon shell (<3 layers), which can effectively prevent the aggregation of Mo<sub>2</sub>C nanocrystals during the high-temperature pyrolysis process and protect the catalyst from corrosion by electrolyte during the catalytic reactions. It is noteworthy that, for a core–shell structure, the shell thickness is of significance to the catalytic activity of the catalysts. According to the reported literature [33], a thick shell (>3 carbon layers) is not conducive to electron permeation to the surface of the catalyst. Hence, the ultrathin carbon shell in this work is beneficial for the electron transfer from the interior Mo<sub>2</sub>C to the carbon surface, which makes a charge redistribution on the exterior carbon shell. The bright spots in the high angle annular dark field scanning transition electron microscope (HAADF-STEM) image indicate the isolated Mo<sub>2</sub>C nanocrystals all over the BNC. The element mappings show that the Mo, C, N and B are homogeneously distributed (Fig. 2d). The Energy Dispersive X-Ray Spectroscopy (EDX) results show the doping contents of B and N are 10.32 and 8.42 wt% (Table S1), respectively, confirming the successful introducing of B and N elements into the catalyst. During the one-pot pyrolysis, the dicyandiamide not only serves as a nitrogen source to generate N-doped carbon shell that encapsulates the Mo<sub>2</sub>C nanocrystal, but also regulates the electronic structure of the catalyst surface and promotes the conductivity and stability of the catalyst. As control, when using glucose as the carbon source, the prepared Mo<sub>2</sub>C@C fails to form a regular morphology and exists in an amorphous material instead (Fig. S1).

XRD, FT-IR and Raman patterns were further employed to explore the detailed structure of the Mo<sub>2</sub>C@BNC. As

shown in Fig. 2e, the peaks centered at 33.6°, 37.4°, 39.5°, 52.1°, 61.6° and 74.8° correspond to the (100), (002), (101), (102), (110) and (112) crystal planes of the hexagonal β-Mo<sub>2</sub>C (PDF#35-0787), respectively. No other peak can be observed in the Mo<sub>2</sub>C@BNC XRD pattern, indicating the boron and nitrogen mainly introduced into the carbon host of the Mo<sub>2</sub>C crystals. In the Raman spectra (Fig. 2f), vibration peaks around at 649.8, 818.7 and 991.1 cm<sup>-1</sup> are fingerprint bands characteristic, confirming the formation of the Mo<sub>2</sub>C phase [34]. Additional peaks located at 1348 and 1595 cm<sup>-1</sup> are attributed to the characteristic D and G bands of carbon materials, respectively. The  $A_{\text{read}}/A_{\text{reaG}}$  ratio increases from 2.2 of the Mo<sub>2</sub>C@NC to 2.4 of the Mo<sub>2</sub>C@BNC, implying that the disorder of the graphite structure increases after the introduction of the extra B atoms [35]. The FT-IR spectrum of the Mo<sub>2</sub>C@BNC sample (Fig. 2g) shows a peak centered at 734 cm<sup>-1</sup>, corresponding to the out-of-plane vibration of the hexagonal B–N bond [36], which is not found in the Mo<sub>2</sub>C@NC spectrum. Besides, the peaks located at 1209.3 and 1297.6 cm<sup>-1</sup> belong to the characteristic C–B bond and C–N bond, respectively [37, 38]. These results confirm the unique structure of the Mo<sub>2</sub>C@BNC, in which the Mo<sub>2</sub>C nanocrystals are encapsulated by an ultrathin B, N dual-doped carbon layer.

XPS analysis reveals the chemical states and electronic structures of the samples. In the Mo 3*d* spectra (Fig. 3a), the peaks at 228.9 and 231.98 eV correspond to the binding energies of Mo<sup>2+</sup>, which are typical characteristics of the Mo<sub>2</sub>C. The peaks at 229.89 and 233.26 eV correspond to the binding energies of Mo<sup>4+</sup>, while the peaks at 232.4 and 235.98 eV correspond to the binding energies of Mo<sup>6+</sup>, respectively, which are assigned to Mo species that oxidized in the preparation process [39, 40]. Compared with that of the Mo<sub>2</sub>C@NC sample, the Mo 3*d* XPS spectrum of the Mo<sub>2</sub>C@BNC presents a positive shift of 0.12 eV. It indicates the enhanced electron delocalization of the interior Mo<sub>2</sub>C after boron introduction, which facilitates the charge redistribution of the exterior BNC shell. In the N 1*s* spectrum (Fig. 3b), four peaks at 395.2, 398.4, 399.6 and 401.5 eV are observed, which can be assigned to the binding energies of Mo 3*p*, pyridinic N, pyrrolic N and graphitic N, respectively, further demonstrating the successful doping of N into the carbon layer. An additional peak is observed at 397.8 eV in the N 1*s* spectrum after B doping, which is attributed to the B–N binding energy [41]. In this work, according to the XPS spectrum, the pyridinic N content of the Mo<sub>2</sub>C@BNC is 38.97%, far greater than that of the Mo<sub>2</sub>C@NC (24.50%), implying that the electron structure

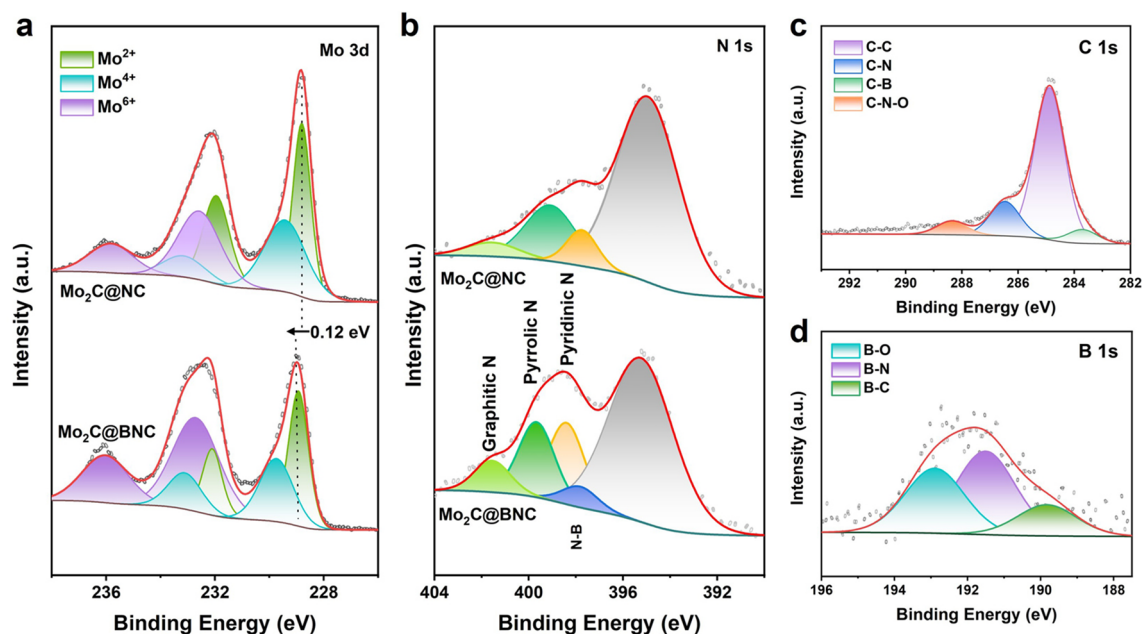


**Fig. 3** XPS spectra of  $\text{Mo}_2\text{C}@NC$  and  $\text{Mo}_2\text{C}@BNC$ : **a**  $\text{Mo } 3d$ . **b**  $\text{N } 1s$ . **c**  $\text{C } 1s$  XPS spectrum of  $\text{Mo}_2\text{C}@BNC$ . **d**  $\text{B } 1s$  XPS spectrum of  $\text{Mo}_2\text{C}@BNC$

of  $\text{Mo}_2\text{C}@BNC$  has been greatly modified (Table S2). This means that the doping of B decorated the electronic structure of the exterior carbon shell. In the  $\text{C } 1s$  spectrum (Figs. 3c and S2), strong peaks can be observed for the C-C species at 284.8 eV, other peaks at 283.7, 286.4 and 288.3 eV correspond to the C-B, C-N and C-N-O binding energies [42]. The  $\text{B } 1s$  spectrum (Fig. 3d) can be observed with three peaks located at 189.8, 191.5 and 192.8 eV, corresponding to the B-C, B-N and B-O binding energies, respectively [43]. The co-existence of the B-C and B-N species indicates the partial replacement of C atoms with B atoms in the carbon layer. It's also affirmed that partial electrons in the  $\text{Mo}_2\text{C}@BNC$  are transferred from Mo to the carbon layer after the introduction of element B, and the dual-doped B and N elements enables the activation of the adjacent C atom due to electron restructuring, facilitating the hydrogen evolution reaction [44].

### 3.2 Electrocatalytic Performance

The HER activities of the prepared  $\text{Mo}_2\text{C}@BNC$  catalyst were determined in 1 M KOH. The catalytic performances of the  $\text{Mo}_2\text{C}@NC$ ,  $\text{Mo}_2\text{C}@C$  and commercial 10% Pt/C catalysts were also measured in the same condition as

control. As shown in Fig. 4a, the designed  $\text{Mo}_2\text{C}@BNC$  catalyst displays an excellent HER catalytic activity with an over potential of 99 mV to deliver the current density of  $10 \text{ mA cm}^{-2}$ , which is significantly lower than those of the  $\text{Mo}_2\text{C}@NC$  (144 mV) and  $\text{Mo}_2\text{C}@C$  (259 mV), indicating that B doping can substantially enhance the HER electrocatalytic activity. We have also investigated the catalytic activity of the  $\text{Mo}_2\text{C}@BNC$  catalysts with various B doping concentrations, provided an optimized B doping level in this study (Fig. S3). Moreover, the  $\text{Mo}_2\text{C}@BNC$  shows a robust catalytic activity at large current density that even superior to the commercial 10% Pt/C catalyst (Fig. 4a, c). The overpotential is 168 mV for  $\text{Mo}_2\text{C}@BNC$  to achieve  $100 \text{ mA cm}^{-2}$ , 20 mV less than that of the commercial 10% Pt/C (188 mV), demonstrating its great potential in industrial applications. The performance of the  $\text{Mo}_2\text{C}@BNC$  surpasses most state-of-the-art reported  $\text{Mo}_2\text{C}$ -based materials (Table S3), addressing one of the best catalytic activities among  $\text{Mo}_2\text{C}$ -based catalysts ever reported.

Furthermore, the Tafel slope is used to study the catalytic kinetics during the reaction process [45]. HER usually comprises two possible steps in alkaline media, as shown in the following equation:

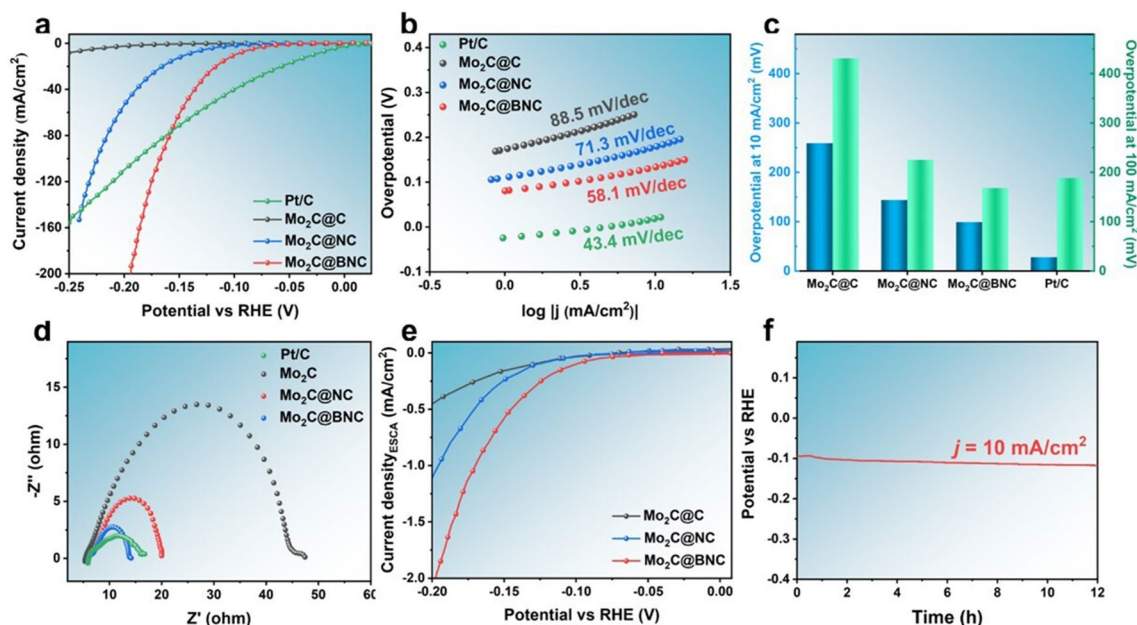
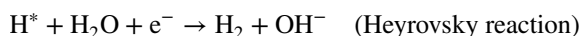
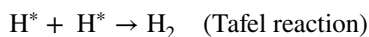


**Fig. 4** HER electrocatalytic properties of the Mo<sub>2</sub>C@BNC catalyst. **a** LSV curves of Mo<sub>2</sub>C@C, Mo<sub>2</sub>C@NC, Mo<sub>2</sub>C@BNC and Pt/C in 1 M KOH electrolyte. **b** Tafel slopes. **c** Overpotentials at 10 and 100 mA cm<sup>-2</sup>. **d** EIS curves. **e** The polarization curves normalized by ECSA. **f** Constant potential V–t curves of Mo<sub>2</sub>C@BNC



or



where H\* refers to the H atom adsorbed on the surface of the catalysts. HER is separated into the water-cleaving (Volmer reaction) and the hydrogen coupling (Tafel reaction or Heyrovsky reaction) steps, resulting in two reaction pathways, namely the Volmer–Heyrovsky or Volmer–Tafel mechanism. In general, the rate-determining step (RDS) can be understood by the Tafel slope, which reflects the electron transfer capacity between the H\* and the catalyst. The Tafel slope of 30 mV dec<sup>-1</sup> shows that the RDS is Tafel step and the reaction follows the Volmer–Tafel pathway. The Tafel slope of 40 mV dec<sup>-1</sup> indicates that the Heyrovsky step is the RDS and the reaction follows the Volmer–Heyrovsky pathway. The Tafel slope of 118 mV dec<sup>-1</sup> means that Volmer step is the RDS and the reaction may follow the Volmer–Heyrovsky or Volmer–Tafel pathway [46]. As shown in Fig. 4b, the calculated Tafel slope of the Mo<sub>2</sub>C@BNC for HER is 58.1 mV dec<sup>-1</sup>, smaller than those of the Mo<sub>2</sub>C@NC (71.3 mV dec<sup>-1</sup>) and Mo<sub>2</sub>C@C (88.5 mV dec<sup>-1</sup>), demonstrating the superior kinetics of the Mo<sub>2</sub>C@BNC among

the catalysts. The Tafel slope value of the Mo<sub>2</sub>C@BNC also implies that the reaction proceeds through a Volmer–Heyrovsky pathway, during which the Heyrovsky step is the rate-determining step. Meanwhile, we further confirm the superior adsorption of Mo<sub>2</sub>C@BNC on H by testing HER performance in acidic solution (Fig. S4). Besides, the EIS results (Fig. 4d) measured at -0.2 V<sub>RHE</sub> confirm that the Mo<sub>2</sub>C@BNC has the smallest charge-transfer resistance in the reaction.

The electrochemically active surface area (ECSA) of the catalyst is measured to further evaluate the effect of surface area on the electrochemical performance. ECSA is proportional to the electrochemical double-layer capacitance (C<sub>dl</sub>) of the material (Fig. S5). The Mo<sub>2</sub>C@BNC shows a great ECSA value, indicating that the B doping can expose more active sites and contribute to the HER catalytic activity [43]. Besides, the polarization curves were normalized by ECSA (J<sub>ECSA</sub>) to explore the effect of intrinsic activity, as shown in Fig. 4e. Mo<sub>2</sub>C@BNC exhibits the highest J<sub>ECSA</sub> among all the samples, demonstrating the intrinsically enhanced activity. The stability of the Mo<sub>2</sub>C@BNC was tested by chronopotentiometry at a constant density of 10 mA cm<sup>-2</sup> (Fig. 4f). There is a tiny increment of potential during the 12 h reaction, and no significant change in the morphology and structure of the catalyst after the durability test (Fig.

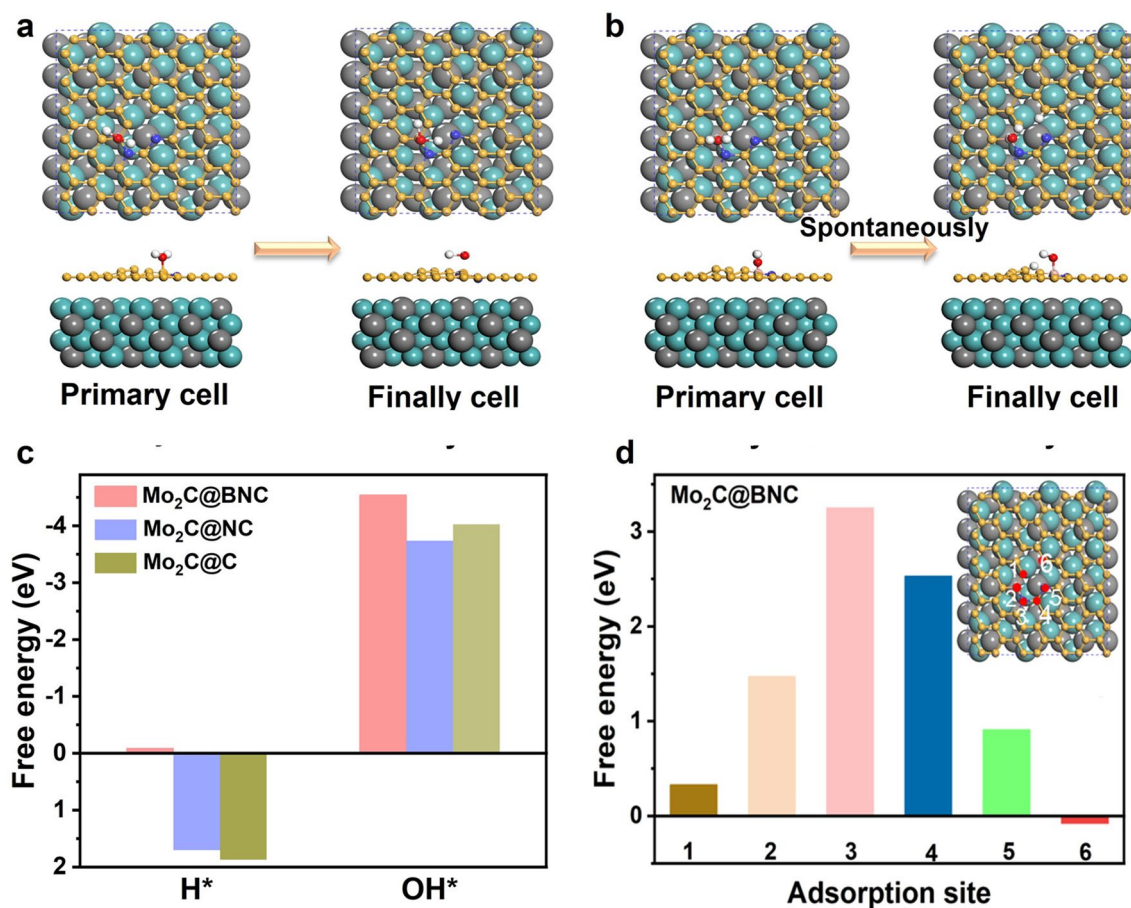


**Fig. 5** DFT calculation results of the HER process on the catalyst surfaces. H<sub>2</sub>O cleaving process on the surfaces of **a** Mo<sub>2</sub>C@NC and **b** Mo<sub>2</sub>C@BNC. **c** OH\* and H\* adsorption energies for the Mo<sub>2</sub>C@NC and Mo<sub>2</sub>C@BNC. **d** Calculated H\* free energy ( $\Delta G_{H^*}$ ) for different sites. Yellow: C atom, blue: N atom, pink: B atom, cyan: Mo atom. (Color figure online)

S6), demonstrating the favorable stability of the catalyst. This is attributed to the fact that the carbon layer is wrapped with Mo<sub>2</sub>C nanocrystals, which can effectively prevent the electrolyte from corroding the catalyst and greatly maintain the catalytic activity [47].

### 3.3 Mechanism Analysis of the Enhanced Catalytic Performance

DFT calculations were performed to gain atomic insights into the synergistic effect of B doping on the HER activity. Figure 5a–b revealed that H<sub>2</sub>O is unfavorable for the adsorption on the Mo<sub>2</sub>C@NC substrate. However, the introduced B endows the superior ability of H<sub>2</sub>O adsorption and the following spontaneous decomposition on the Mo<sub>2</sub>C@BNC. This is confirmed by the hydrophilicity test

of the samples. Mo<sub>2</sub>C@BNC possessed the best hydrophilicity with a water contact angle of 20.4°, which was smaller than that of Mo<sub>2</sub>C@NC (25.41°, Fig. S7), confirming the Mo<sub>2</sub>C@BNC exhibits better hydrophilicity than the Mo<sub>2</sub>C@NC. During this process, the reaction intermediates H\* and OH\* are prone to be adsorbed on the defective C site and B site, respectively. To identify the detailed roles of the dopants in the reaction, we calculated the possible adsorption of H\* and OH\* species on the theoretical models. As shown in Fig. 5c, the free energy for H\* adsorption ( $\Delta G_{H^*}$ ) on Mo<sub>2</sub>C@C surface is evaluated to be 1.87 eV, which is quite unfavorable for the hydrogen evolution reaction (Fig. S8a). The  $\Delta G_{H^*}$  on Mo<sub>2</sub>C@NC surface is 1.7 eV, implying that the N dopants could adjusted the electron distribution of external carbon layer, thus slightly improving the free energy of H\*



adsorption (Fig. S9a). In contrast, the Mo<sub>2</sub>C@BNC displays a Pt-like H\* adsorption energy of  $-0.085$  eV (the C site) after B doping, which is an optimal state close to a thermo-neutral value. Furthermore, H\* free energies on different adsorption sites for the Mo<sub>2</sub>C@BNC surface were calculated to identify the active site in the reaction (the insert in Fig. 5d). The chosen theoretical model for the Mo<sub>2</sub>C@BNC is shown in the inset of Fig. 5d, in which the C site adjacent to B (Fig. S9b) is the most effective site for H\* adsorption (Fig. 5d). The significantly improved adsorption ability is attributed to the Co-introduction of B and N. When the electrons transfer from Mo to the carbon layer, due to the different electronegativity ( $B < C < N$ ), the electrons will be redistributed between those non-metallic atoms, which can effectively activate the C atoms, making it a near-zero H\* adsorption Gibbs free energy.

Furthermore, the doping of B also strengthens the adsorption energy of OH\* (Fig. 5c). The best adsorption site for OH\* of the Mo<sub>2</sub>C@C and Mo<sub>2</sub>C@NC sample is the C site that near the H\* adsorption site (Figs. S8b and S9c). After B doping, the electron-deficient B atoms adsorbs water by coordinating with the lone pair of electrons, thus weakening the O–H bond to accelerate water dissociation. The best reaction center on the Mo<sub>2</sub>C@BNC surface becomes the B site (Fig. S9d). This is evidenced by the distance between the O atom from H<sub>2</sub>O and the active sites. It is calculated that the distance between the O atom and the adsorbed C site ( $d_{O-C}$ ) is  $1.71$  Å for Mo<sub>2</sub>C@C and  $2.186$  Å for Mo<sub>2</sub>C@NC. The value changes to  $1.457$  Å for the distance between the O atom and the adsorbed B site ( $d_{O-B}$ ) for Mo<sub>2</sub>C@BNC. As a result, the adsorption energy of the OH\* increases from  $-4.0$  and  $-3.74$  eV over the primary C site to  $-4.54$  eV over the B site. The enhanced adsorption energy of H\* and OH\* after the introduction of B is more favorable for H<sub>2</sub>O decomposition, which is clarified from the changes of density of projection state (DOS) of the Mo<sub>2</sub>C@BNC and Mo<sub>2</sub>C@NC samples (Fig. S10). Compared with the B-free sample, the H\*-C and OH\*-B interactions are strengthened in the B-doping sample. In short, DFT calculations confirm that the B doping greatly enhances the Volmer reaction in the HER process, making water cleaves into H\* and OH\*. At the same time, the inert C atom is activated together with the B and N atoms and facilitated the Heyrovsky step. The synergistic effect between these non-metal B site and C site over the carbon shell thus greatly improving the HER activity.

## 4 Conclusions

In summary, we have designed a Mo<sub>2</sub>C@BNC catalyst that N, B dual-doped ultrathin carbon shell encapsulated on Mo<sub>2</sub>C nanocrystals. The doping of N and B elements coupled with defects on the surface of the carbon layer, generates multiple active centers, which significantly enhances HER activity compared to the pristine samples. This catalyst delivers a current density of  $10$  mA cm<sup>-2</sup> with a very low over-potential of  $99$  mV. More importantly, the catalytic activity even exceeds that of the commercial Pt/C catalyst at large current density, addressing one of the best non-noble metal based HER catalyst in alkaline solutions. Theoretical calculations reveal that the introduction of B can trigger the spontaneous decomposition of H<sub>2</sub>O and facilitate the Volmer reaction, simultaneously activating the adjacent C atom, resulting in a near-zero regulation of  $\Delta G_{H^*}$ . This paper demonstrates the importance of multiple active centers concerning the alkaline HER activity and provides fresh insight to explore the acceleration of water dissociation via the effect of boron.

**Acknowledgements** This work is supported by the National Natural Science Foundation of China (Grant No. 52202310), Natural Science Foundation of Jiangsu Province (Grant No. BK20191443), the Qinglan Project, Youth Hundred Talents Program and the Top-talent Program of Yangzhou University, the Innovation technology platform project (YZ2020268) jointly built by Yangzhou City and Yangzhou University, Postgraduate Research & Practice Innovation Program of Jiangsu Province (SJCX22\_1703), the Key Research and Development Projects of Sichuan Province (23ZDYF0466), “Tianfu Emei” Science and Technology Innovation Leader Program in Sichuan Province and University of Electronic Science and Technology of China Talent Start-up Funds (A1098 5310 2360 1208).

**Funding** Open access funding provided by Shanghai Jiao Tong University.

### Declarations

**Conflict of interest** The authors declare that they have no known competing financial interests or personal relationships that could have appeared to influence the work reported in this paper.

**Open Access** This article is licensed under a Creative Commons Attribution 4.0 International License, which permits use, sharing, adaptation, distribution and reproduction in any medium or format, as long as you give appropriate credit to the original author(s) and the source, provide a link to the Creative Commons licence, and indicate if changes were made. The images or other third party material in this article are included in the article’s Creative

Commons licence, unless indicated otherwise in a credit line to the material. If material is not included in the article's Creative Commons licence and your intended use is not permitted by statutory regulation or exceeds the permitted use, you will need to obtain permission directly from the copyright holder. To view a copy of this licence, visit <http://creativecommons.org/licenses/by/4.0/>.

**Supplementary Information** The online version contains supplementary material available at <https://doi.org/10.1007/s40820-023-01135-0>.

## References

- C. Li, N. Clament Sagaya Selvam, J. Fang, Shape-controlled synthesis of platinum-based nanocrystals and their electrocatalytic applications in fuel cells. *Nano-Micro Lett.* **15**, 83 (2023). <https://doi.org/10.1007/s40820-023-01060-2>
- B. Jiang, D. Tian, Y. Qiu, X. Song, Y. Zhang et al., High-index faceted nanocrystals as highly efficient bifunctional electrocatalysts for high-performance lithium–sulfur batteries. *Nano-Micro Lett.* **14**, 40 (2022). <https://doi.org/10.1007/s40820-021-00769-2>
- Y. Yang, Y. Yu, J. Li, Q. Chen, Y. Du et al., Engineering ruthenium-based electrocatalysts for effective hydrogen evolution reaction. *Nano-Micro Lett.* **13**, 160 (2021). <https://doi.org/10.1007/s40820-021-00679-3>
- R. Li, H. Xu, P. Yang, D. Wang, Y. Li et al., Synergistic interfacial and doping engineering of heterostructured NiCo(OH)<sub>x</sub>-Co<sub>y</sub>W as an efficient alkaline hydrogen evolution electrocatalyst. *Nano-Micro Lett.* **13**, 120 (2021). <https://doi.org/10.1007/s40820-021-00639-x>
- B. Guo, Y. Ding, H. Huo, X. Wen, X. Ren et al., Recent advances of transition metal basic salts for electrocatalytic oxygen evolution reaction and overall water electrolysis. *Nano-Micro Lett.* **15**, 57 (2023). <https://doi.org/10.1007/s40820-023-01038-0>
- Z. Chen, X. Duan, W. Wei, S. Wang, B.J. Ni, Iridium-based nanomaterials for electrochemical water splitting. *Nano Energy* **78**, 105270 (2020). <https://doi.org/10.1016/j.nanoen.2020.105270>
- Q. Yin, C.L. Hill, Water splitting: passing the acid test. *Nat. Chem.* **10**(1), 6–7 (2017). <https://doi.org/10.1038/nchem.2921>
- F. Lu, M. Zhou, Y. Zhou, X. Zeng, First-row transition metal based catalysts for the oxygen evolution reaction under alkaline conditions: basic principles and recent advances. *Small* **13**(45), 1701931 (2017). <https://doi.org/10.1002/sml.20170193>
- J.N. Tiwari, S. Sultan, C.W. Myung, T. Yoon, N. Li et al., Multicomponent electrocatalyst with ultralow Pt loading and high hydrogen evolution activity. *Nat. Energy* **3**(9), 773–782 (2018). <https://doi.org/10.1038/s41560-018-0209-x>
- C. Xie, W. Chen, S. Du, D. Yan, Y. Zhang et al., In-situ phase transition of WO<sub>3</sub> boosting electron and hydrogen transfer for enhancing hydrogen evolution on Pt. *Nano Energy* **71**, 104653 (2020). <https://doi.org/10.1016/j.nanoen.2020.104653>
- J. Chen, Y. Ha, R. Wang, Y. Liu, H. Xu et al., Inner Co synergizing outer ru supported on carbon nanotubes for efficient pH-universal hydrogen evolution catalysis. *Nano-Micro Lett.* **14**, 186 (2022). <https://doi.org/10.1007/s40820-022-00933-2>
- Q. Cheng, C. Hu, G. Wang, Z. Zou, H. Yang et al., Carbon-defect-driven electroless deposition of Pt atomic clusters for highly efficient hydrogen evolution. *J. Am. Chem. Soc.* **142**(12), 5594–5601 (2020). <https://doi.org/10.1021/jacs.9b11524>
- J. Zhang, E. Wang, S. Cui, S. Yang, X. Zou et al., Single-Atom Pt anchored on oxygen vacancy of monolayer Ti<sub>3</sub>C<sub>2</sub>T<sub>x</sub> for superior hydrogen evolution. *Nano Lett.* **22**(3), 1398–1405 (2022). <https://doi.org/10.1021/acs.nanolett.1c04809>
- M. Zhou, H. Li, A. Long, B. Zhou, F. Lu et al., Modulating 3d orbitals of Ni atoms on Ni-Pt edge sites enables highly-efficient alkaline hydrogen evolution. *Adv. Energy Mater.* **11**(36), 2101789 (2021). <https://doi.org/10.1002/aenm.202101789>
- B. Šljukić, M. Vujković, L. Amaral, D.M.F. Santos, R.P. Rocha et al., Carbon-supported Mo<sub>2</sub>C electrocatalysts for hydrogen evolution reaction. *J. Mater. Chem. A* **3**(30), 15505–15512 (2015). <https://doi.org/10.1039/c5ta02346g>
- Y. Qiu, Z. Wen, C. Jiang, X. Wu, R. Si et al., Rational design of atomic layers of Pt anchored on Mo<sub>2</sub>C nanorods for efficient hydrogen evolution over a wide pH range. *Small* **15**(14), e1900014 (2019). <https://doi.org/10.1002/sml.201900014>
- W. Fu, Y. Wang, W. Tian, H. Zhang, J. Li et al., Non-metal single-phosphorus-atom catalysis of hydrogen evolution. *Angew. Chem. Int. Ed.* **59**(52), 23791–23799 (2020). <https://doi.org/10.1002/ange.202011358>
- H. Vrubel, X. Hu, Molybdenum boride and carbide catalyze hydrogen evolution in both acidic and basic solutions. *Angew. Chem. Int. Ed.* **51**(51), 12703–12706 (2012). <https://doi.org/10.1002/anie.201207111>
- X. Yang, J. Cheng, X. Yang, Y. Xu, W. Sun et al., Facet-tunable coral-like Mo<sub>2</sub>C catalyst for electrocatalytic hydrogen evolution reaction. *Chem. Eng. J.* **451**(4), 138977 (2023). <https://doi.org/10.1016/j.cej.2022.138977>
- Y. Shi, B. Zhang, Recent advances in transition metal phosphide nanomaterials: synthesis and applications in hydrogen evolution reaction. *Chem. Soc. Rev.* **45**(6), 1529–1541 (2016). <https://doi.org/10.1039/c5cs00434a>
- J. Greeley, T.F. Jaramillo, J. Bonde, I.B. Chorkendorff, J.K. Nørskov, Computational high-throughput screening of electrocatalytic materials for hydrogen evolution. *Nat. Mater.* **5**(11), 909–913 (2006). <https://doi.org/10.1038/nmat1752>
- F. Yu, Y. Gao, Z. Lang, Y. Ma, L. Yin, Electrocatalytic performance of ultrasmall Mo<sub>2</sub>C affected by different transition metal dopants in hydrogen evolution reaction. *Nanoscale* **10**(13), 6080–6087 (2018). <https://doi.org/10.1039/c8nr00908b>
- C. Wan, B.M. Leonard, Iron-doped molybdenum carbide catalyst with high activity and stability for the hydrogen evolution reaction. *Chem. Mater.* **27**(12), 4281–4288 (2015). <https://doi.org/10.1021/acs.chemmater.5b0062>

24. H. Wei, J. Wang, Q. Lin, Y. Zou, X. Chen et al., Incorporating ultra-small N-doped Mo<sub>2</sub>C nanoparticles onto 3D N-doped flower-like carbon nanospheres for robust electrocatalytic hydrogen evolution. *Nano Energy* **86**, 106047 (2021). <https://doi.org/10.1016/j.nanoen.2021.106047>
25. Y. Lu, C. Yue, Y. Li, W. Bao, X. Guo et al., Atomically dispersed Ni on Mo<sub>2</sub>C embedded in N, P co-doped carbon derived from polyoxometalate supramolecule for high-efficiency hydrogen evolution electrocatalysis. *Appl. Catal. B Environ.* **296**, 120336 (2021). <https://doi.org/10.1016/j.apcatb.2021.120336>
26. D. Wang, T. Liu, J. Wang, Z. Wu, N, P(S) Co-doped Mo<sub>2</sub>C/C hybrid electrocatalysts for improved hydrogen generation. *Carbon* **139**, 845–852 (2018). <https://doi.org/10.1016/j.carbon.2018.07.043>
27. Y. Liu, G. Yu, G.D. Li, Y. Sun, T. Asefa et al., Coupling Mo<sub>2</sub>C with nitrogen-rich nanocarbon leads to efficient hydrogen-evolution electrocatalytic sites. *Angew. Chem. Int. Ed.* **127**(37), 10902–10907 (2015). <https://doi.org/10.1002/ange.201504376>
28. T.T. Yang, W.A. Saidi, Graphene activation explains the enhanced hydrogen evolution on graphene-coated molybdenum carbide electrocatalysts. *J. Phys. Chem. Lett.* **11**(7), 2759–2764 (2020). <https://doi.org/10.1021/acs.jpcclett.0c00615>
29. G. Chen, T. Wang, J. Zhang, P. Liu, H. Sun et al., Accelerated hydrogen evolution kinetics on NiFe-layered double hydroxide electrocatalysts by tailoring water dissociation active sites. *Adv. Mater.* **30**(10), 1706279 (2018). <https://doi.org/10.1002/adma.201706279>
30. S. Ye, F. Luo, T. Xu, P. Zhang, H. Shi et al., Boosting the alkaline hydrogen evolution of Ru nanoclusters anchored on B/N-doped graphene by accelerating water dissociation. *Nano Energy* **68**, 104301 (2020). <https://doi.org/10.1016/j.nanoen.2019.104301>
31. D.S. Baek, J. Lee, J. Kim, S.H. Joo, Metastable phase-controlled synthesis of mesoporous molybdenum carbides for efficient alkaline hydrogen evolution. *ACS Catal.* **12**(12), 7415–7426 (2022). <https://doi.org/10.1021/acscatal.2c01772>
32. Y. Lin, M. Zhou, X. Tai, H. Li, X. Han et al., Analytical transmission electron microscopy for emerging advanced materials. *Matter* **4**(7), 2309–2339 (2021). <https://doi.org/10.1016/j.matt.2021.05.005>
33. H. Jiang, L. Yan, S. Zhang, Y. Zhao, X. Yang et al., Electrochemical surface restructuring of phosphorus-doped carbon@ MoP electrocatalysts for hydrogen evolution. *Nano-Micro Lett.* **13**(1), 215 (2021). <https://doi.org/10.1007/s40820-021-00737-w>
34. Y. Huang, Q. Gong, X. Song, K. Feng, K. Nie et al., Mo<sub>2</sub>C nanoparticles dispersed on hierarchical carbon microflowers for efficient electrocatalytic hydrogen evolution. *ACS Nano* **10**(12), 11337–11343 (2016). <https://doi.org/10.1021/acsnano.6b0658>
35. G. Qian, J. Chen, T. Yu, J. Liu, L. Luo et al., Three-phase heterojunction NiMo-based nano-needle for water splitting at industrial alkaline condition. *Nano-Micro Lett.* **14**(1), 20 (2022). <https://doi.org/10.1007/s40820-021-00744-x>
36. T. Zhang, G. Wen, X. Huang, B. Zhong, H. Yu, Preparation of high purity BCN hollow spheres by pyrolyzing a simple polymeric precursor. *CrystEngComm* **12**(11), 3506–3510 (2010). <https://doi.org/10.1039/c003714a>
37. X. Yu, P. Han, Z. Wei, L. Huang, Z. Gu et al., Boron-doped graphene for electrocatalytic N<sub>2</sub> reduction. *Joule* **2**(8), 1610–1622 (2018). <https://doi.org/10.1016/j.joule.2018.06.007>
38. A. Dogra, I. Barlocco, A. Singh, F. Somodi, A. Villa et al., Metal free alkene hydrogenation by B-doped graphitic carbon nitride. *Catal. Sci. Technol.* **10**(9), 3024–3028 (2020). <https://doi.org/10.1039/d0cy00488j>
39. R. Ma, Y. Zhou, Y. Chen, P. Li, Q. Liu et al., Ultrafine molybdenum carbide nanoparticles composited with carbon as a highly active hydrogen-evolution electrocatalyst. *Angew. Chem. Int. Ed.* **127**(49), 14936–14940 (2015). <https://doi.org/10.1002/ange.201506727>
40. H. Li, F. Yu, X. Ling, H. Wan, M. Zhang et al., Dual-cation-doped MoS<sub>2</sub> nanosheets accelerating tandem alkaline hydrogen evolution reaction. *Nanotechnology* **32**(44), 445703 (2021). <https://doi.org/10.1088/1361-6528/ac17c5>
41. J.S. Li, Y. Wang, C.H. Liu, S.L. Li, Y.G. Wang et al., Coupled molybdenum carbide and reduced graphene oxide electrocatalysts for efficient hydrogen evolution. *Nat. Commun.* **7**(1), 11204 (2015). <https://doi.org/10.1038/ncomms11204>
42. H. Tabassum, R. Zou, A. Mahmood, Z. Liang, S. Guo, A catalyst-free synthesis of B, N co-doped graphene nanostructures with tunable dimensions as highly efficient metal free dual electrocatalysts. *J. Mater. Chem. A* **4**(42), 16469–16475 (2016). <https://doi.org/10.1039/c6ta07214c>
43. H. Zhang, Z. Ma, J. Duan, H. Liu, G. Liu et al., Active sites implanted carbon cages in core-shell architecture: highly active and durable electrocatalyst for hydrogen evolution reaction. *ACS Nano* **10**(1), 684–694 (2016). <https://doi.org/10.1021/acsnano.5b05728>
44. H. Xu, H. Jia, B. Fei, Y. Ha, H. Li et al., Charge transfer engineering via multiple heteroatom doping in dual carbon-coupled cobalt phosphides for highly efficient overall water splitting. *Appl. Catal. B Environ.* **268**, 118404 (2020). <https://doi.org/10.1016/j.apcatb.2019.118404>
45. X. Wang, Y. Zheng, W. Sheng, Z.J. Xu, M. Jaroniec et al., Strategies for design of electrocatalysts for hydrogen evolution under alkaline conditions. *Mater. Today* **36**, 125–138 (2020). <https://doi.org/10.1016/j.mattod.2019.12.003>
46. T. Shinagawa, A. Garcia-Esparza, K. Takanebe, Insight on Tafel slopes from a microkinetic analysis of aqueous electrocatalysis for energy conversion. *Sci. Rep.* **5**, 13801 (2015). <https://doi.org/10.1038/srep13801>
47. M.A.R. Anjum, M.H. Lee, J.S. Lee, Boron- and nitrogen-codoped molybdenum carbide nanoparticles imbedded in a BCN network as a bifunctional electrocatalyst for hydrogen and oxygen evolution reactions. *ACS Catal.* **8**(9), 8296–8305 (2018). <https://doi.org/10.1021/acscatal.8b01794>